Demonstration of Initial GlennICE Relative Frame Capability: Axial-Flow Propeller

David L. Rigby
HX5 LLC, Cleveland, OH, 44135

Paul H. von Hardenberg
NASA Glenn Research Center, Cleveland, OH, 44135

Modifications have been implemented in the GlennICE software to accommodate a non-inertial reference frame. GlennICE accepts a flow solution from an external flow solver. It then introduces particles and tracks them through the flow field in a Lagrangian manner. Centrifugal and Coriolis terms were added to the GlennICE software to account for relative frame simulations. The objective of the present paper is twofold. First, to check that the new terms are implemented correctly and that the code still behaves as expected with respect to convergence. And second, to provide some initial insight into an upcoming propeller experiment in the NASA Icing Research Tunnel. The paper presents a description of the code modifications. In addition, results are presented for two operating conditions, and three particle sizes. Each case was simulated with four different grid densities to assess grid dependence.

I. Nomenclature

AoA = propeller angle of attack at ¾ (0.75) span along blade (ignoring propeller induction effects) [degrees]
D = propeller diameter [m]
$\boldsymbol{F_{cen}}$ = centrifugal force [kg m/s^2]
$\boldsymbol{F_{cor}}$ = Coriolis force [kg m/s^2]
LWC = icing cloud liquid water content [g/m^3]
m = particle mass [kg]
N = motor rpm
P_{exit} = exit static pressure [Pa]
$P_{tot,in}$ = inlet total pressure [Pa]
$\boldsymbol{r}$ = radius [m]
t = icing exposure time [s]
$T_{tot,in}$ = inlet total temperature [K]
$\mathbf{V}_\infty$ = tunnel speed [m/s]
$\boldsymbol{V_{relative}}$ = relative velocity [m/s]
$\mathbf{V_{tip}}$ = relative velocity of airflow seen by the blade at the tip (considering tunnel speed and rotation velocity) [m/s]
x = axial direction [m]
Beta = collection efficiency [-]
$\beta_{0.75}$ =blade pitch at ¾ span along blade
$\boldsymbol{\omega}$ = rotation rate [radians/s]

II. Introduction

A recent Analysis of Alternatives (AoA) study [1] has demonstrated a need to enable analyses of icing on rotating components. Examples are the fan and spinner, as well as rotors within the compressor. Additionally, there are needs to investigate Advanced Air Mobility (AAM) vehicles and rotorcraft [1]. In the absolute frame, a rotating component presents an unsteady flow field. However, with appropriate assumptions, the flow field can look steady when riding on the rotating component. Anchoring the viewpoint to the rotating component means that additional terms must be introduced to account for the non-inertial reference frame.

The flow solver, that supplies the solution for input to GlennICE, includes the additional non-inertial terms, and now GlennICE also includes terms to account for centrifugal and Coriolis forces.

The paper includes a description of the modifications to the software. It also includes simulations of a four bladed propeller at two different operating conditions. Three particle sizes of 5, 20, and 80 microns were simulated at the two operating conditions. To assess grid dependence, four similar grids were used with increasing refinement. The grid sizes range from 2 million to 31.25 million cells.

III. Methodology

GlennICE has been in development for several years [2-5]. It accepts a flow solution, then uses Lagrangian trajectory simulation to approximate the collection efficiency. Once the collection efficiency is determined, an energy balance is performed on the icing surface and ice growth is approximated.

In the present study, a four bladed propeller is simulated as shown in Figure 1. The geometry is modeled after a configuration that is expected to be tested in the NASA Icing Research Tunnel (IRT) in the near future.

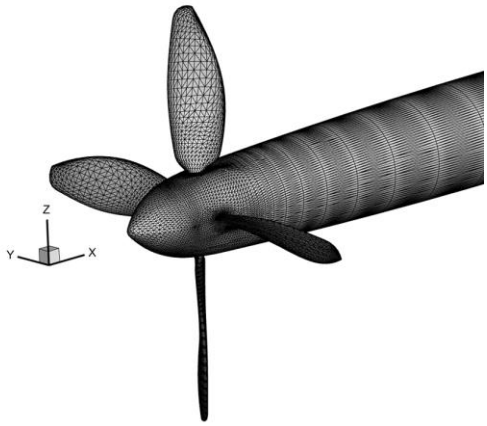

Figure 1. View of propeller configuration.

The nominal twist and chord distributions of the propeller blade geometry were developed by NASA during a design optimization effort to improve acoustic and aerodynamic performance [6]. However, the “as manufactured” geometry differed from the nominal blade design. For the purposes of this study, the “as manufactured” geometry was used so that future comparisons with experimental data can be made. Comparisons of the nominal and “as manufactured” chord and twist distributions are show in Figures 2a and 2b.

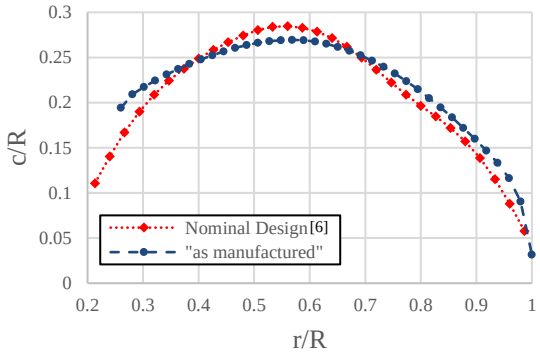

Figure 2a. Nominal vs manufactured chord distributions

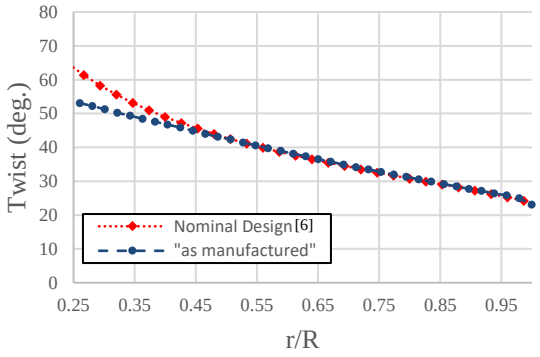

Figure 2b. Nominal vs manufactured twist distributions

The airfoil profile is NACA 0012 throughout the majority of the blade span, however, deviations occur near the root of the blade to enable connection to the hub.

A full ring simulation is performed to eliminate the need for periodic boundary conditions, which are still in development.

In addition to the blades, the spinner geometry matches that of the spinner to be tested in the IRT. The downstream center body is kept axisymmetric to simplify the numerical analysis.

The geometry is initially specified as a Step file [7]. Next, components are extracted using the Rhino software [8] and exported as stereolithography (stl) files [9]. Then, the grid is generated using the GridPro [10] software from Program Development Corporation. The grid is then passed through the Pointwise [11] software to create an unstructured grid.

The flow is generated using the NASA FUN3D [12] software.

The flow solution from FUN3D is then supplied to the GlennICE software to simulate collection efficiency. Then, based on the local water collection on the surface, ice is grown.

The operation of the GlennICE software in the inertial frame has been previously established and documented [4]. In this work, additional terms have been added to the Lagrangian trajectory integration. Two additional contributions to the force on the particle are centrifugal force and Coriolis force.

The equation for the centrifugal force is:

$$\boldsymbol{F}_{cen} = -m\boldsymbol{\omega}\times(\boldsymbol{\omega}\times\boldsymbol{r})$$

The centrifugal force always points radially outward. It is the force that pushes you against the car door as you round a corner.

The equation for the Coriolis force component is:

$\boldsymbol{F_{cor}} = -2m(\boldsymbol{\omega} \times \boldsymbol{V_{relative}})$

Where:

m=$particle\ mass$ [kg]
$\boldsymbol{\omega}$=$\boldsymbol{rotation\ rate}$ [radians/s]
$\boldsymbol{r}$=$\boldsymbol{radius}$ [m]
$\boldsymbol{V_{relative}}$=$velocity\ in\ the\ relative\ frame$ [m/s]

The Coriolis force is the reason that hurricanes rotate one direction in the northern hemisphere, and the opposite direction in the southern hemisphere.

Figure 3 shows an example of a particle trajectory, in the relative frame, that just misses the upper blade.

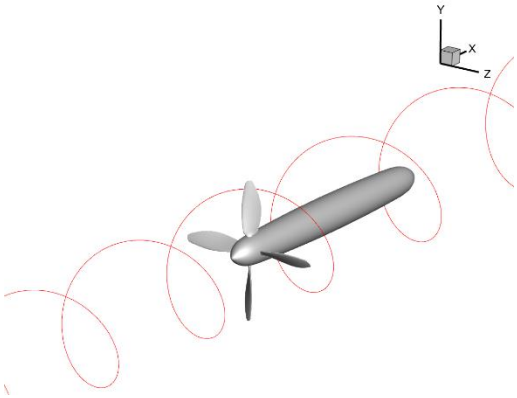

Figure 3. Example of particle trajectory in the relative frame.

IV. Operating Conditions

Table 1 gives a summary of the three operating conditions expected to be investigated experimentally. For the present study, only operating condition 1 (OC1) and operating condition 3 (OC3) were simulated. The conditions OC1 and OC3 were chosen for simplicity since they can use the same grid. Compared to OC1, OC3 has the same relative angle of attack but is running slower (i.e., the tunnel speed and rpm are reduced).

Table 1. Operating conditions investigated.

Operating Condition (OC)	V_∞ (knots | m/s)	$\beta_{0.75}$ (deg.)	N (rpm)	D (in | m)	AoA (deg.)	V_{tip} (knots | m/s)
OC1	130 | 66.9	50.72	1635	36 | 0.914	2	200.2 | 103
OC2	130 | 66.9	52.72	1635	36 | 0.914	4	200.2 | 103
OC3	87 | 44.8	50.72	1094	36 | 0.914	2	133.9 | 68.9

$\mathbf{V_\infty}$ - Tunnel speed
$\beta_{0.75}$ – Blade pitch at ¾ (0.75) span along blade (Figure 4 shows the definition of this angle)
N – motor rpm
D – propeller diameter
AoA – propeller angle of attack at ¾ (0.75) span along blade (ignoring propeller induction effects)
$\mathbf{V_{tip}}$ is the relative velocity of airflow seen by the blade at the tip (considering tunnel speed and rotation velocity)

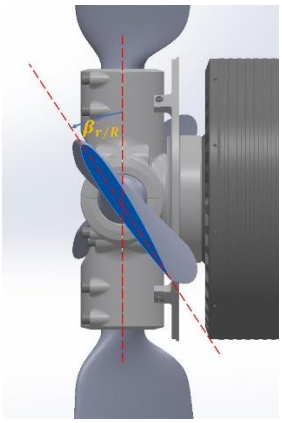

Figure 4. View showing pitch angle definition.

V. Description of cases and boundary conditions

Four similar grids were generated to assess grid dependence. The four grids will be referred to as 1p00X, 1p50X, 2p00X and 2p50X. The name of the grid refers to the increase in refinement in each of the three directions. The initial grid, 1p00X, is first created as a structured multi-block grid. The refined grids are then created by increasing the number of cells in each of the three index directions. Table 2 shows the refinement level and number of cells for each grid.

Table 2. Summary of grids

Grid Name	Refinement Value	Number of Cells [millions]
1p00X	1.00	2.
1p50X	1.50	6.75
2p00X	2.00	16.
2p50X	2.50	31.25

The simulation inlet is placed 9 meters upstream of the center body leading edge. The exit is located 11 meters downstream of the center body leading edge. An outer cylindrical boundary with a diameter of 6 meters was used. Recall that the propeller diameter is 0.914 meters. The propeller and center body are set to no-slip. The outer boundary is set to slip.

At the inlet, total pressure and total temperature are specified. At the exit, static pressure is specified. The pressure ratio is set to achieve the desired through flow velocity. The temperature is set very cold to ensure that only Rime ice occurs (i.e., no runback). The handling of runback water in the non-inertial reference frame is currently under development in GlennICE.

For each operating point, the propeller and center body are run first at a wall temperature of 0.95 times the inlet total temperature, and then at 1.05 times the inlet total temperature. These two solutions are then provided to the GlennICE software to solve for the heat transfer coefficient.

Table 3. Boundary conditions

Operating Condition	Inlet Total Pressure $P_{tot,in}$, [Pa]	Inlet Total Temperature $T_{tot,in}$, [K]	Exit Static Pressure P_{exit}, [Pa]
OC1	95,805	231	93,066
OC3	94,297	231	93,066

For each operating point, three single bin simulations were performed with the GlennICE software. Particle sizes of 5, 20, and 80 microns were investigated. For the ice growth simulation, a value of 1.2 g/m^3 was used for liquid water content (LWC). Ice was allowed to grow for an icing exposure time, t, of 300 seconds.

The FUN3D calculations were carried out on the NASA's Advanced Supercomputing Sstem (NAS). The FUN3D simulation was run as compressible and turbulent. The turbulence model used was sst-v. The largest grid, 2p50X, took roughly 5 hours using 512 Haswell processors at NAS. All solutions were converged to a residual level of 1.e-12.

For the GlennICE simulations, the following parameters were used. The FRACTION_CONTAINED_TOL=0.5, MAX_FACE_HITS=300. This combination allows the leading edge CFD faces to converge while limiting the number of hits that can be amassed near the impingement limits. The refinement levels were continued until the leading edge values of collection, Beta, converged to at least 4 decimal places. This process generally resulted in more than 90% of hit CFD faces reporting converged. Any remaining faces were observed to be near the impingement limit. The faces near the impingement limit are inherently difficult to converge. At the same time, they are of less importance due to low water flux. It is expected that all of the CFD faces that have appreciable water collection are converged long before the impingement limit is converged.

VI. Introductory Results

Figure 5 shows an example of the seed plane, as well as the surface geometry colored by collection efficiency. The seed plane is located at the simulation inlet. Each point on the seed plane represents a location where a trajectory was released. The GlennICE code starts from a very coarse seed plane grid and then automatically releases points in regions to converge the collection efficiency without wasting too many points that will miss the icing surface. Confirming that the addition of non-inertial terms appears to cause no disruption in the convergence was one of the objectives of the current study.

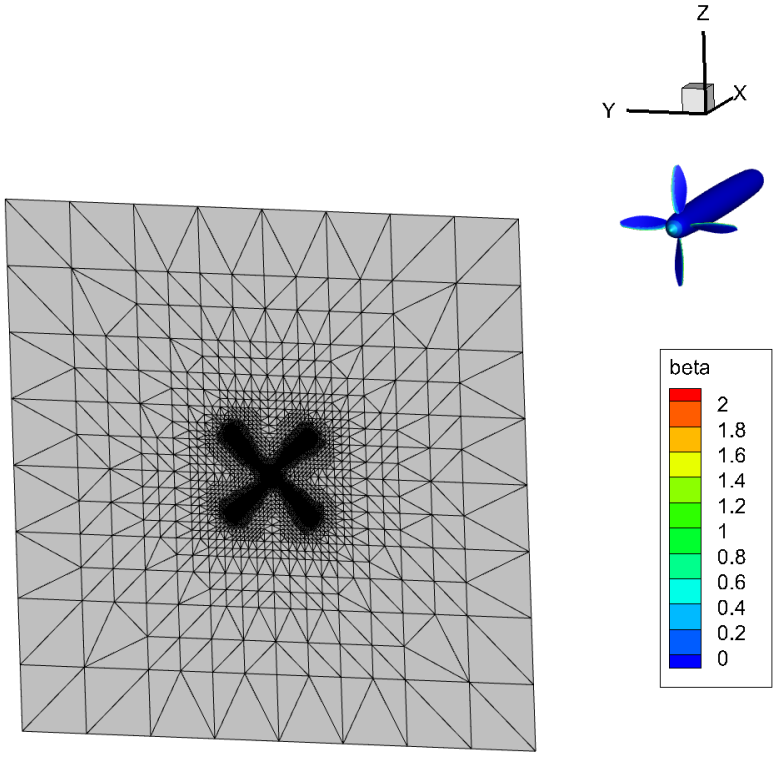

Figure 5. Upstream seed plane and icing surfaces colored by collection.

Figure 6 shows a zoomed in view of the seed plane. The observed clustering of release points is as expected based on previous inertial reference frame simulations.

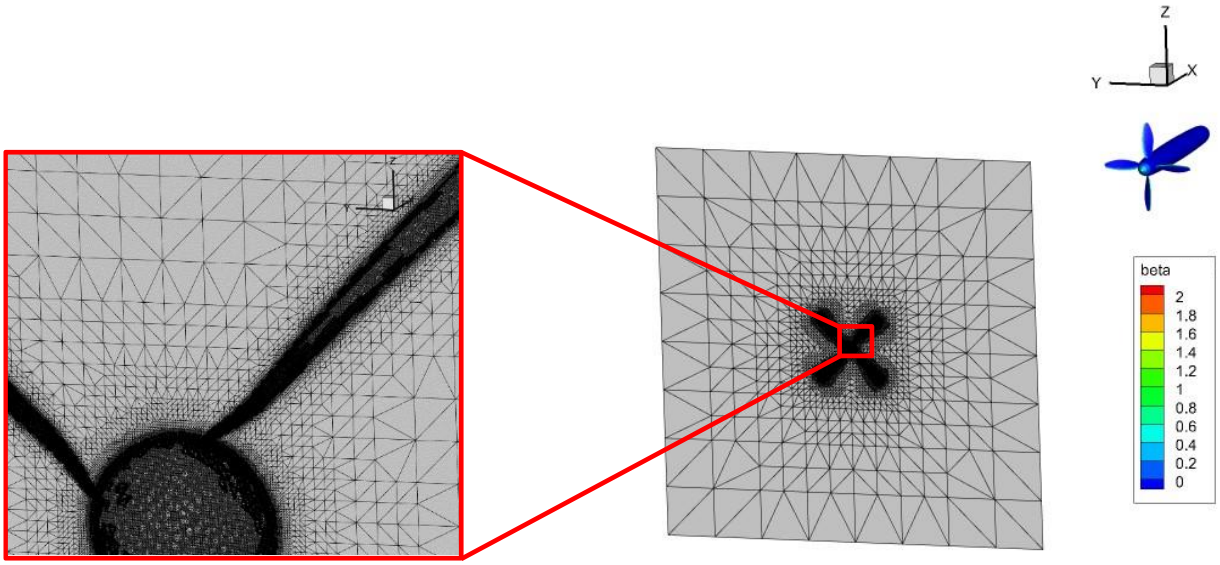

Figure 6. Zoomed in view of seed plane.

Figure 7 shows a zoomed in view of the propeller. The collection efficiency has the expected distribution. A level below one is expected at the nose of the center body. Additionally, higher values are expected on the blade leading edges. At the outer radius of the blade, values greater than one are possible, owing to the high relative velocity.

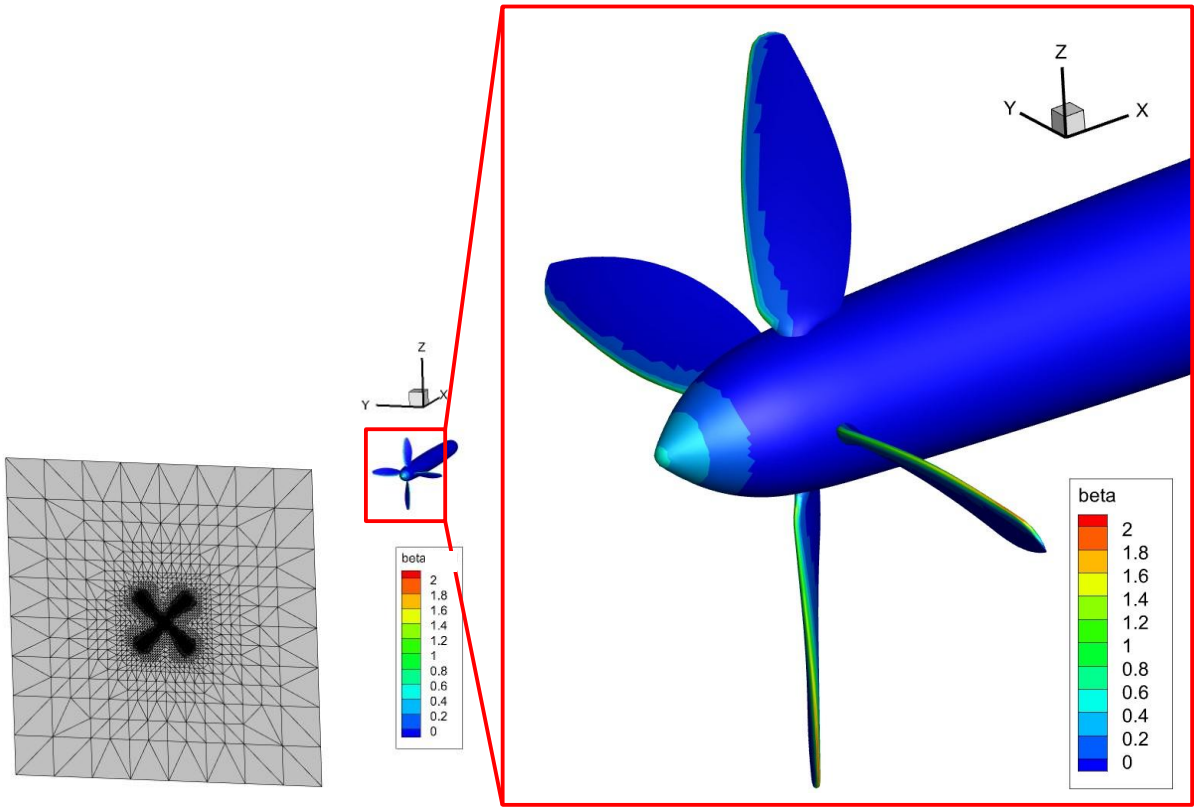

Figure 7. Zoomed in view of collection.

Figure 8 shows an example of the ice growth in blue. This result is for OC1 and particle size 20 microns and the finest grid of 2p50X.

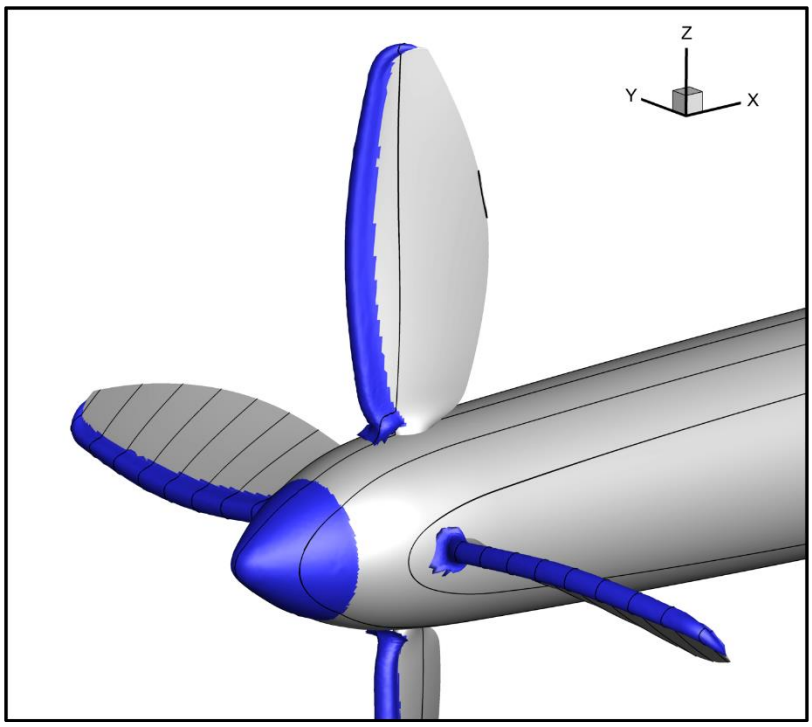

Figure 8. Ice growth shown in blue

Figure 9 shows the same result as Figure 8, except that the blue ice surface is removed. With the ice surface removed, it is possible to see the cross-section of the three-dimensional ice shape at various y-locations.

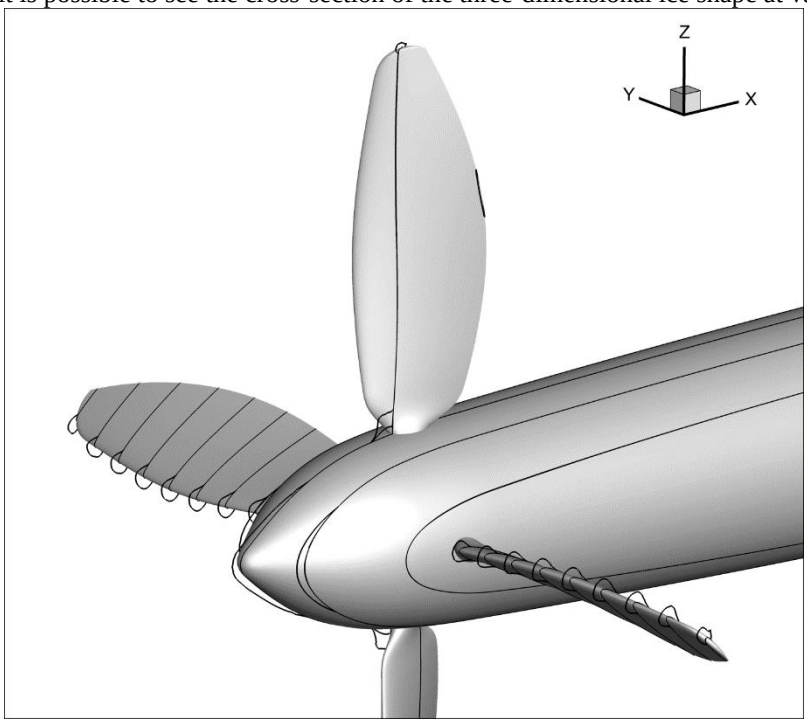

Figure 9. Black lines showing the ice growth cross sections at various values of Y.

VII. Grid Dependence

To assess grid dependence, two areas will be investigated. First, a cut at the ¾ span location (0.3429 m) will show the pressure distribution and water collection (Beta). Then, Beta along the center body and leading edge of the propeller will be shown.

Figure 10 shows the pressure distribution for OC1 at the ¾ span location. It can be seen that the 1p00X grid is too coarse as the peak pressure and the trailing edge pressure differ from the finer grids. It can also be seen that the 2p50X and 2p00X grids have good agreement.

Figure 11 shows the collection efficiency, Beta, at the same ¾ span location as Figure 10. Notice that the x-direction range has been reduced to highlight the impingement region. Figure 11 indicates that grid 1p00X is too coarse and that the 2p50X grid is in good agreement with the next coarser 2p00X grid.

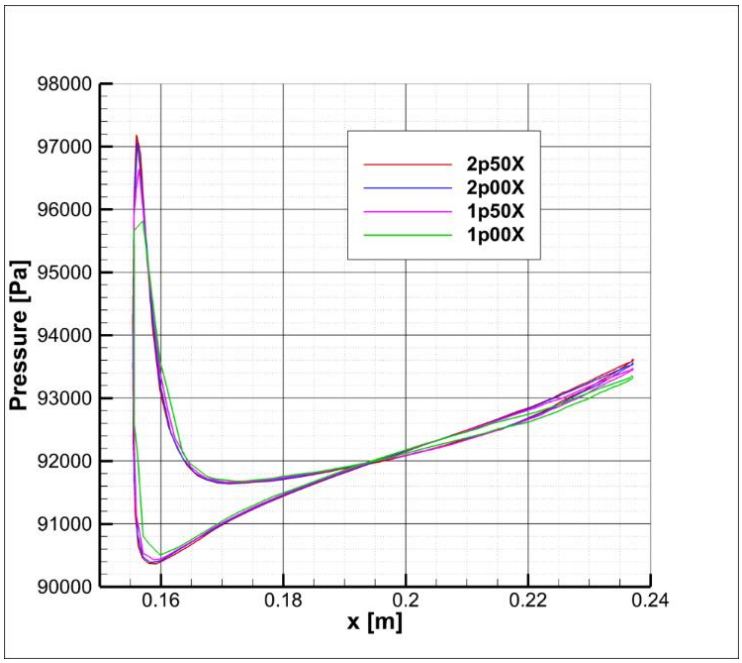

Figure 10. Cut at 75% span. OC1, 20 microns.

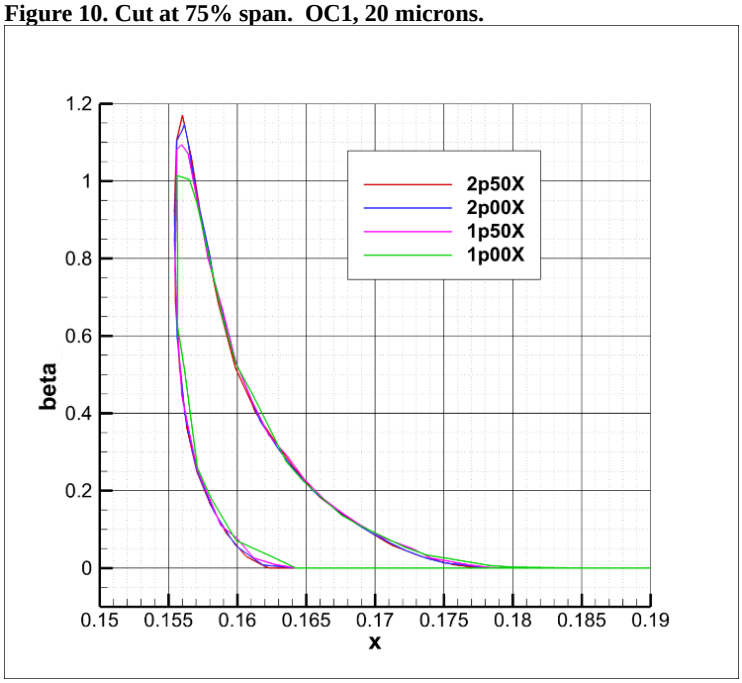

Figure 11. Cut at 75% span. OC1, 20 microns. Note change in x range to highlight impingement region.

Figure 12 shows the collection efficiency along the center body and along the leading edge of the propeller. Figure 12a is included to demonstrate the geometry location relative to the plot values of Beta in Figure 12b.

Tecplot was used to extract the data for Figure 12b in the following ways.

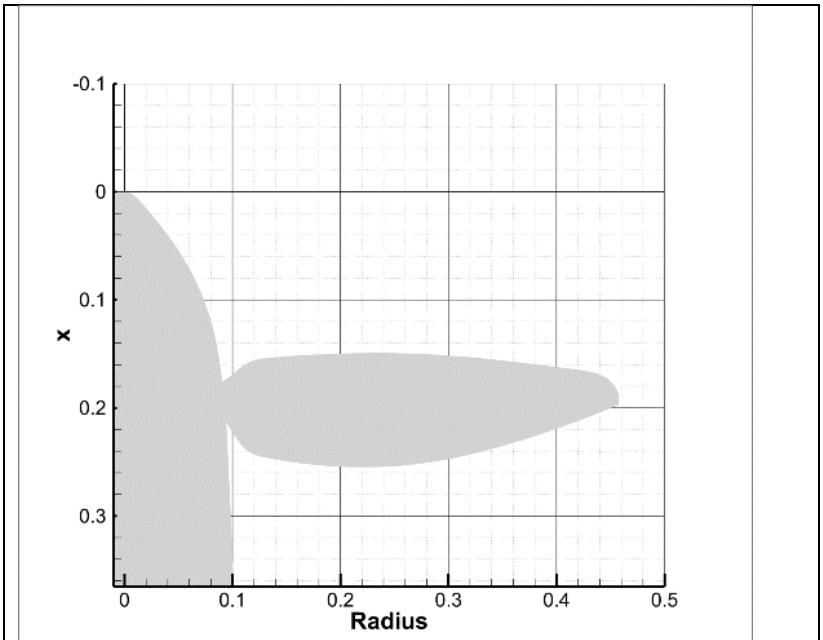

Figure 12a. Planform of geometry to help visualizing the figure below.

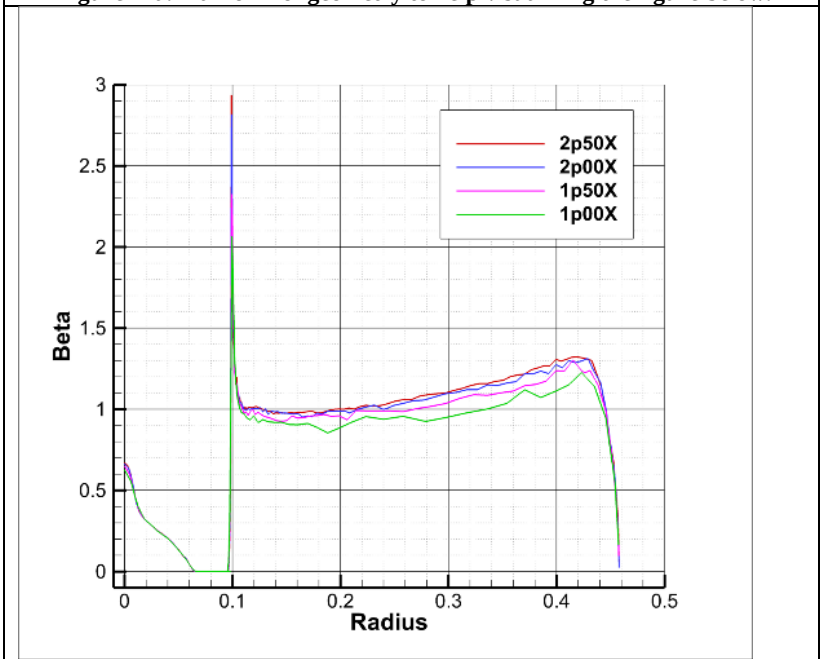

Figure 12b. Collection efficiency for OC1, 20 microns case.

On the center body the minimum and maximum values of radius and Beta were extracted for 2000 x-locations between 0 and 0.3 m. The minimum and maximum values were then added and divided by two to produce radius and Beta pairs from the center body leading edge to downstream of the propeller.

On the propeller, 2000 y-slices were made between the propeller root and tip. At each y-slice the maximum value of Beta was extracted. The value of y for the slice was used for the radius in the radius and Beta pairs along the propeller leading edge. Note that the actual location of the maximum Beta for a given y-slice can be at a slightly different radius. However, it was deemed that y and radius could be used interchangeably because the difference will be quite small.

The results in Figure 12b demonstrate that the finest grid, 2p50X, is sufficiently refined to provide acceptable results. The results on the center body (radius between 0 and 0.1 m) agree for all of the grids, except near the center body leading edge. The results along the leading edge of the propeller show a steady progress toward grid convergence as the grids are refined. The 20 microns case produces a shadow zone near the root of the propeller and a highly concentrated zone at the edge of the shadow zone (near Radius=0.1 m). The peak value of the spike near Radius=0.1 is 2.07, 2.33, 2.82, and 2.93, for the grids 1p00X, 1.50X, 2p00X, and 2p50X, respectively. The changes in the peak value get progressively smaller and the difference between 2p00X and 2p50X is less than 4%.

Figure 13 shows a closer look at the center body region. Figure 13 shows that most of the center body result is in very good agreement, even for the coarsest grid. Additionally, it can be seen that the leading edge value is converging.

The conclusion from the comparison of four grids is that the finest grid is certainly providing acceptable results.

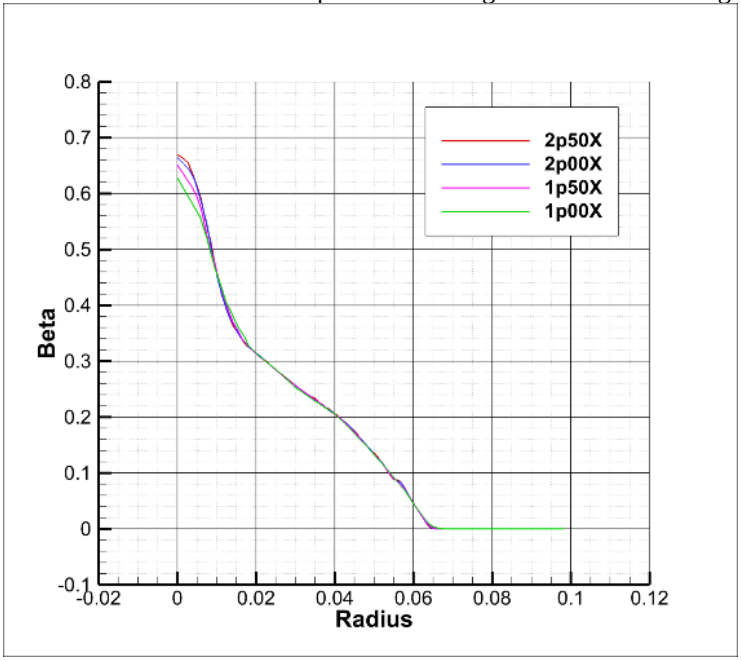

Figure 13. OC1, 20 microns. Zoomed in on center body

VIII. Fine Grid Results

Results are now presented for the 2p50X grid. For each of the two operating points, OC1 and OC2 described in Table 1, three particle sizes were simulated. Values for particle diameter of 5, 20, and 80 microns were investigated.

Figure 14 shows the collection efficiency across the center body and propeller leading edge for OC1 (the higher speed case). The trends are as expected, with some exceptions that will be discussed below. On the center body, it can be seen that the peak value increases with increasing particle size. In addition, the impingement region grows larger as particle size increases. The value of Beta drops rapidly at the high curvature region of the nose near the centerline and then more slowly further from the centerline over the conical portion of the nose. Finally, Beta drops rapidly again to the impingement limit as the curvature increases approaching the propeller. Now focusing on the propeller leading edge portion of Figure 14 (i.e., 0.1<Radius<0.46) we see some interesting results. The peak value along the propeller leading edge generally increases with particle size, as expected. It also increases as the radius increases, owing to the increased relative velocity at the larger radius. Near the root of the propeller (i.e., near Radius=0.1), an interesting phenomenon occurs. Both the 5 microns and the 80 microns case impinge all the way to the root. However, the 20 microns case has a shadow zone and a sharp spike.

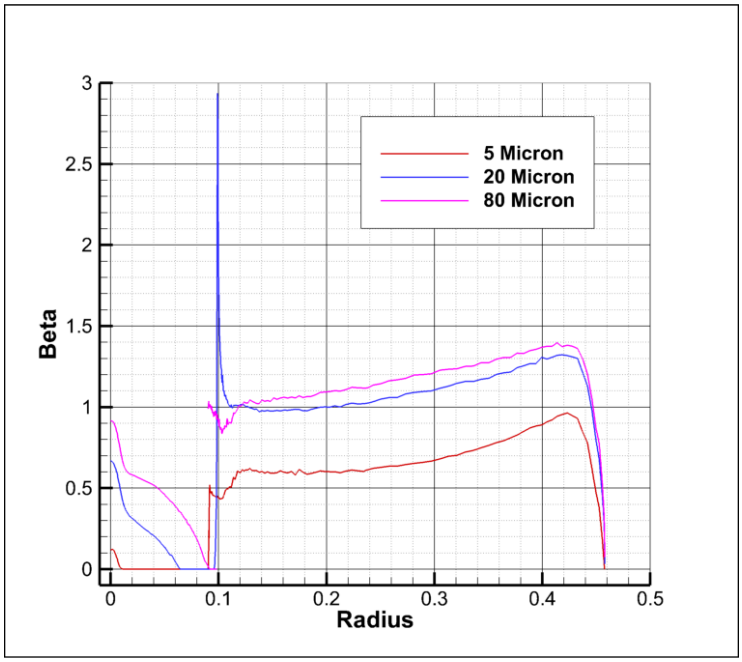

Figure 14. OC1, 2p50X. Notice 20 microns has shadow zone near propeller root, but both 5 and 80 microns have no shadow zone.

Figure 15 presents the results for OC3 (the lower speed case). Trends are very similar to the results for OC1 shown in Figure 14. Owing to the lower tunnel speed and lower RPM, the values of Beta are generally reduced. All other trends are the same as Figure 15, with one small exception; there is a small amount of collection on the center body near the propeller root for the 5 microns case. None of the other 5 cases had collection on the center body near the root of the propeller. The only indication in Figure 15 is a small red spike near Radius=0.095. In a later figure showing ice shape (Figure 17), the small ice growth on the center body near the propeller root will be visible.

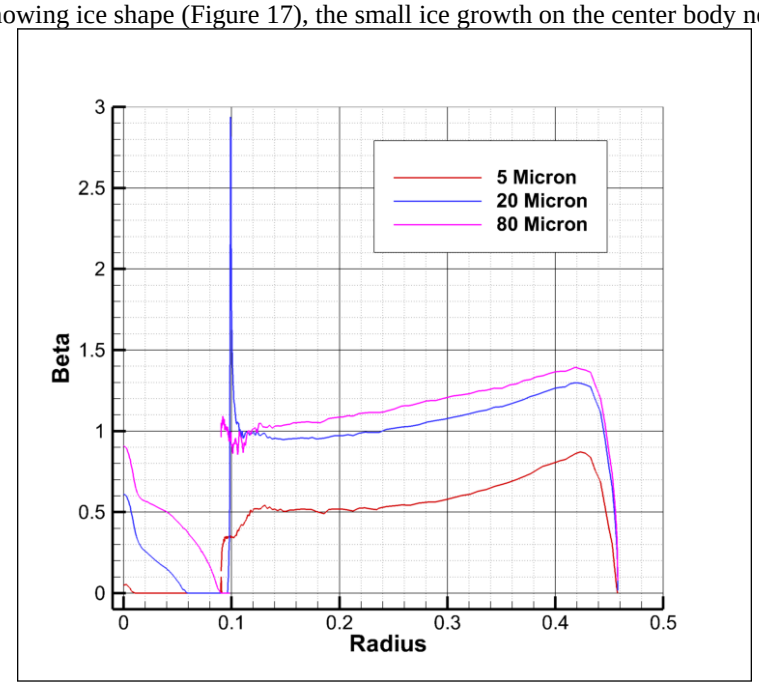

Figure 15. OC3, 2p50X. Similar to OC1 at somewhat reduces levels of Beta. Little tick of red near x=0.09 shows slight collection on center body near root of propeller. The OC3, 5 microns case is the only case to have any collection in that area.

Figure 16 shows the ice shape for each of the 6 conditions (2 operating points and 3 particle sizes). Figure 16a and 16b show the 5 microns results for OC1 and OC3, respectively. At 5 microns the impingement region is relatively small for both center body and propeller.

Figure 16c and 16d show the results of the 20 microns simulations for OC1 and OC3, respectively. Impingement regions are significantly increased relative to 5 microns. The impingement limit on the center body is farther back for OC1 due to the higher freestream velocity. On the propeller, it is interesting to note the shadow zone at the root and the spike in thickness just above the shadow zone.

Figure 16e and 16f shows the results for 80 microns results for OC1 and OC3, respectively. Compared to the 20 microns cases the impingement zones are significantly increased. Once again, the impingement limit is farther back for OC1, compared to OC3, since it is the higher speed case.

Figure 17 shows a close up view of the ice on the center body near the root of the propeller for the OC3, 5 microns case. Interestingly, this is the only case to have collection at the root of the propeller. At the same time, however, it is such a small amount that it is probably not very important in this case.

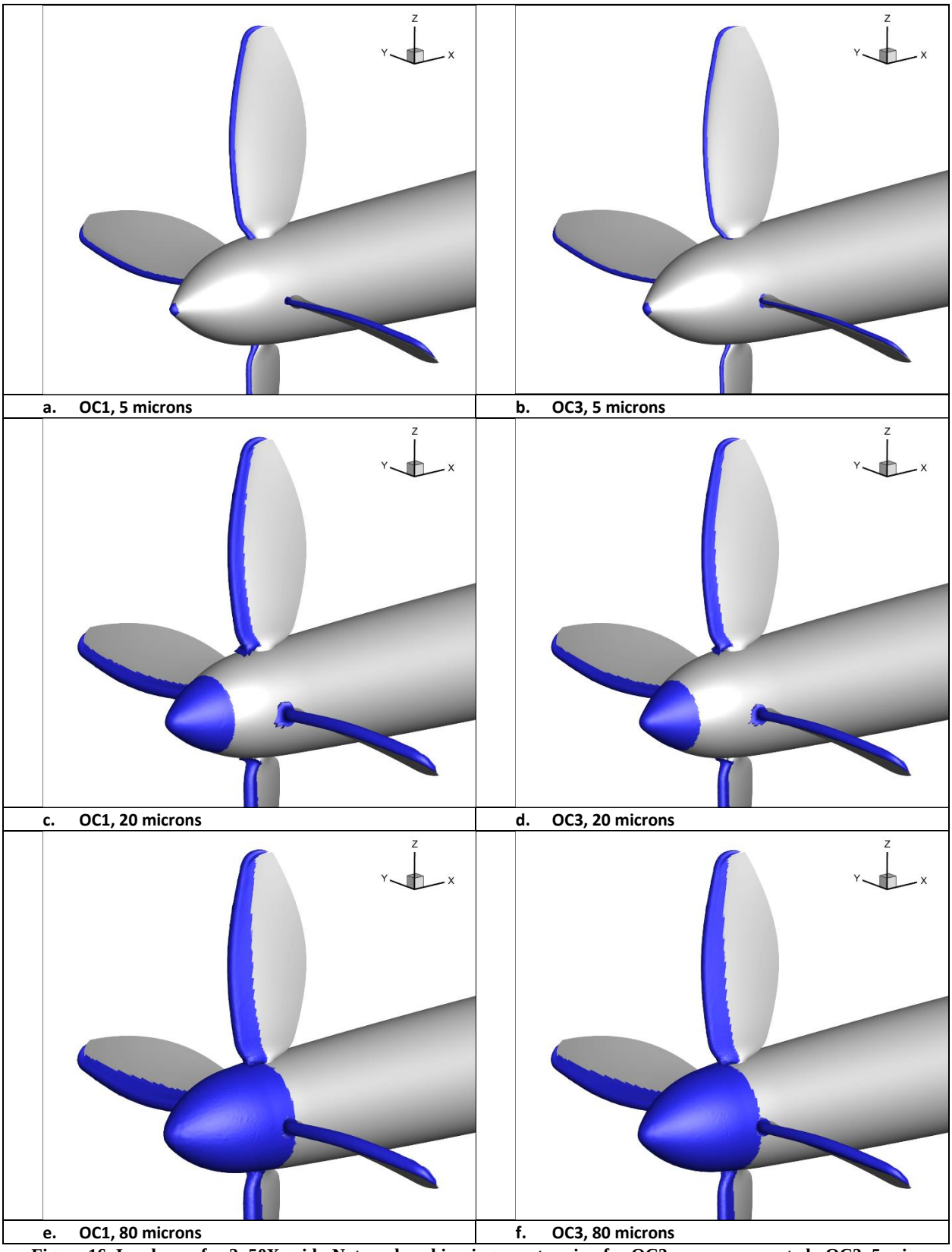

Figure 16. Ice shapes for 2p50X grid. Note reduced impingement region for OC3 cases, as expected. OC3, 5 microns case is the only case to show some ice on the center body near the root of the propeller.

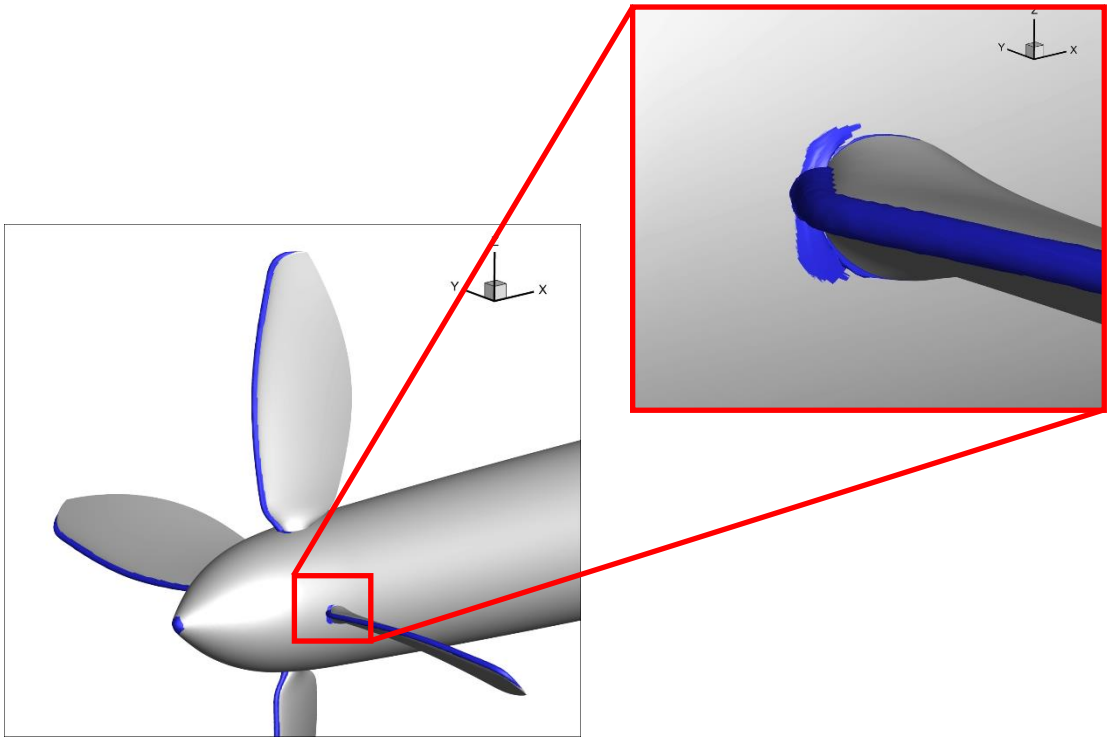

Figure 17. Ice shape for OC3, 5 microns. Only case to produce ice on center body near propeller root.

IX. Summary

The present work describes the implementation and testing of the addition of the non-inertial frame capability in the GlennICE software. A set of sample results are presented demonstrating the expected behavior. The sample case represents a propeller in axial flow. The propeller geometry is expected to be tested in the NASA IRT at similar operating conditions in the near future. By observing a single particle trajectory in the relative frame, and seeing the expected helical path, it was confirmed that the new Force terms were implemented properly. In addition, observing how the GlennICE software converged to a final result confirmed that all of the techniques that have worked for inertial frame still work in the relative frame. Comparing results from four different grid resolutions confirmed that the fine grid results are acceptable. Comparing collection for three different particle sizes and two operating points demonstrated expected trends. Operating condition 1 (OC1) and operating condition 3 (OC3) have the same relative angle of attack, with OC1 run having a higher axial speed and RPM than OC3. The collection efficiency results consistently produced larger values for OC1 relative to OC3 at the same particle size. Also, OC1 consistently produced larger impingement regions when compared to OC3. Both larger collection efficiency and larger impingement region for OC1 are consistent with expectations.

The observed behavior of collection efficiency as particle size varied also agreed with expectations. That is to say, larger particles produced larger values of collection efficiency and larger impingement zones.

Two interesting phenomena were observed. The first was a shadow zone and spike in collection efficiency near the root of the propeller for the 20 microns cases. This will be discussed more in the next paragraph. The second was the small amount of collection observed on the center body near the root of the propeller for one specific case. The OC3 with 5 microns particles was the only case to produce collection on the center body near the propeller. The collection is so small that it probably does not matter from a practical point of view, but it will be of interest to see if the phenomena is observed experimentally.

The 20 microns case, for both OC1 and OC3, produced a shadow zone and spike on the propeller near the root This phenomenon was not observed for either the 5 microns or 80 microns cases. The conclusion from this would be that there is a limited range of particle size that produce a shadow zone. Once again, it will be interesting to see if this phenomenon is observed experimentally.

Finally, ice shapes were shown for the six cases (2 operating conditions, and 3 particle sizes). The liquid water content (LWC) was 1.2 [g/m^3] and icing exposure time, t, was 300 seconds. These cases were run very cold to generate rime shapes which essentially create a spatial representation of the collection efficiency. The ice shapes also provide a useful visualization of the impingement limits and show the spike in collection efficiency for the 20 microns cases.

Overall, these results are very encouraging. It is expected that many additional simulations will be run in the future to support the experimental effort.

Acknowledgments

This work is supported by the NASA Advanced Air Transport Technology Project (AATT), the Transformation Tools and Technologies (TTT) project, and Revolutionary Vertical Lift Technology Project (RVLT). Calculations were performed at the NASA Advanced Supercomputing (NAS) Division. This work would not be possible without the efforts of others on the GlennICE Team. GlennICE Team members currently include Eric Galloway, Christopher Porter, Thomas Ozoroski, David Rigby and Zaid Sabri.

References

[1] "NASA Analysis of Alternatives Study for Icing Research", NASA/TM-20220006956, September 2020.

[2] Porter, C.E., "A Comparison of Trajectory Refinement Schemes for GlennICE." *AIAA AVIATION Forum 2022*. AIAA 2022-3692. 2022.

[3] Porter, C.E., "Three Dimensional Surface Redefinition Method for Computational Ice Accretion Solvers." *AIAA AVIATION Forum 2020.* AIAA 2020-2831. 2020.

[4] Wright, W.B., Porter, C.E., Galloway, E.T. and Rigby, D.L. ``GlennICE 2.1 capabilities and results," AIAA AVIATION 2022 Forum, 2022.

[5] Wright, W.B., Porter, C.E., Galloway, E.T. and Rigby, D.L., ``An automated refinement process for particle trajectory methods in GlennICE," AIAA 2021-2631, 2021.

[6] Zawodny, N.S., Pettingill, N.A., Leonard, V.L., and Ingraham, D.J., "Experimental Validation of an Acoustically and Aerodynamically Optimized UAM Proprotor Part 1: Test Setup and Results," Tech. Rep. NASA TM 20220015637, NASA Langley Research Center, Hampton, VA, United States, February 2023.

[7] "STEP (File Format)" https://en.wikipedia.org/wiki/ISO_10303-21.

[8] "Rhino3D", www.rhino3d.com.

[9] "STL (File Format)" Wikipedia, Wikimedia Foundation, 13 June 2020, https://en.wikipedia.org/wiki/STL_(file_format).

[10] GridPro Program Development Corporation, www.gridpro.com.

[11] Pointwise, Software Package, V18.2R2, Pointwise Inc., Fort Worth, TX, 2019.

[12] FUN3D, Software Package, V13.7, NASA Langley Research Center, Hampton, VA, 2021.